

ARTICLE OPEN



Tandem GCIB-ToF-SIMS and GCIB-XPS analyses of the 2-mercaptobenzothiazole on brass

Matjaž Finšgar¹✉

Surface analysis of 2-mercaptobenzothiazole (MBTH) adsorbed on brass from 3 wt.% NaCl solution was performed by means of X-ray photoelectron spectroscopy and tandem (MS/MS) time-of-flight secondary ion mass spectrometry (ToF-SIMS). These surface analytical techniques were used in association with the gas cluster ion beam (GCIB) sputtering method at various acceleration energies and cluster sizes, which slowly removes the surface layer and leaves the chemical information intact during the sputtering of the very thin surface layer. In addition, MS¹ ToF-SIMS was used for 2D and 3D imaging to show the molecular and elemental distribution of the surface species. Using the tandem ToF-SIMS capability, the MS² spectra clearly confirmed the presence of MBTH on the surface. Moreover, organometallic complexes were indicated, which formed between the MBTH and Cu ions released due to the corrosion of the brass. These analyses were performed based on the fragmentation products identified in the MS² spectra.

npj Materials Degradation (2023)7:1; <https://doi.org/10.1038/s41529-022-00317-2>

INTRODUCTION

The X-ray photoelectron spectroscopy (XPS) technique, and lately also the time-of-flight secondary ion mass spectrometry (ToF-SIMS) technique, are essential for determining the surface properties of a solid material. The functionalities of the materials can be governed by either their surface properties or the properties of the bulk material. In most cases, both play an important role in the final performance of the material. A detailed surface analysis, carried out in order to obtain the elemental- and molecular-specific information of the very thin surface layers, is virtually impossible without XPS and ToF-SIMS. Lately, the development of the gas cluster ion beam (GCIB) sputter source has been recognized as having different possibilities in the analysis of organic materials^{1,2}.

ToF-SIMS is a surface analytical technique that provides both elemental and molecular information. However, quantitative information is limited with ToF-SIMS, while XPS provides quantitative information. The use of GCIB in association with ToF-SIMS measurements can provide 3D imaging without chemically destroying the organic material and thus provides valuable information in an organic material investigation, e.g., the spatial distribution of the molecular species in the solid material. Even though ToF-SIMS has a very high mass resolution, one still might encounter spectral interferences—signals at a very similar mass-to-charge (m/z) ratio, which can lead to analytical misinterpretation. Some studies can report that a particular analyte was present but actually fragments of some other species were detected, and vice versa. This is a very serious and dangerous analytical problem. The solution to such may be the use of the tandem (MS/MS) capability by transmitting the fragment at a particular m/z to the second analyzer and determining its structure, or at least rejecting the possible predicted structure. After obtaining reliable signal information, 2D- and 3D-imaging can be performed with both MS¹ and MS². Tandem ToF-SIMS has not been widely employed in the corrosion and corrosion inhibition research community, probably due to this technique's rare availability.

Brass is one of the most commonly used metallic materials due to its advantageous mechanical properties in various applications, such as water distribution networks for manufacturing fasteners, fittings, and pipes³. Corrosion of brass, like other metallic materials, depends on the environment to which it is exposed^{4,5}. For example, corrosion of brass becomes more problematic in solutions containing chlorides^{6,7}. One way to mitigate the corrosion of brass in chloride solutions is to use corrosion inhibitors. One such corrosion inhibitor is 2-mercaptobenzothiazole (MBTH), which was shown previously to effectively mitigate the corrosion of copper and brass^{8–14}.

This work describes the surface properties of the MBTH surface layer formed on brass when immersed in 3 wt.% NaCl solution containing MBTH. MBTH is considered to be a corrosion inhibitor that mitigates brass corrosion in 3 wt.% NaCl solution^{15–25}. A corrosion inhibitor is a chemical compound dissolved in the corrosive medium at low concentrations that adsorbs on the surface of the metallic material and forms a surface layer which mitigates the corrosion process. For that reason, the corrosion inhibition effectiveness of MBTH was first proven after 31 days of immersion by a surface examination of the brass sample in 3 wt.% NaCl solution containing 100 ppm MBTH using field-emission scanning electron microscopy (FE-SEM), atomic force microscopy (AFM), and 3D-profilometry. Moreover, the hydrophobic character of this surface layer was checked by contact angle measurements. Next, the study focused on investigating, by means of tandem ToF-SIMS and XPS, the surface layer that formed initially on the brass surface. ToF-SIMS and XPS were used in association with the GCIB sputter source to determine the depth profiles using molecular and elemental specific signals. The formation of organometallic complexes between the MBTH and the metal ions was investigated using tandem ToF-SIMS by detailed investigation of the MS² spectra.

RESULTS AND DISCUSSION

Corrosion and surface properties after 31 days of immersion

A 3 wt.% NaCl solution is highly corrosive to brass and, therefore, a suitable model solution to test the corrosion inhibition effect of

¹University of Maribor, Faculty of Chemistry and Chemical Engineering, Smetanova ulica 17, 2000 Maribor, Slovenia. ✉email: matjaz.finsgar@um.si

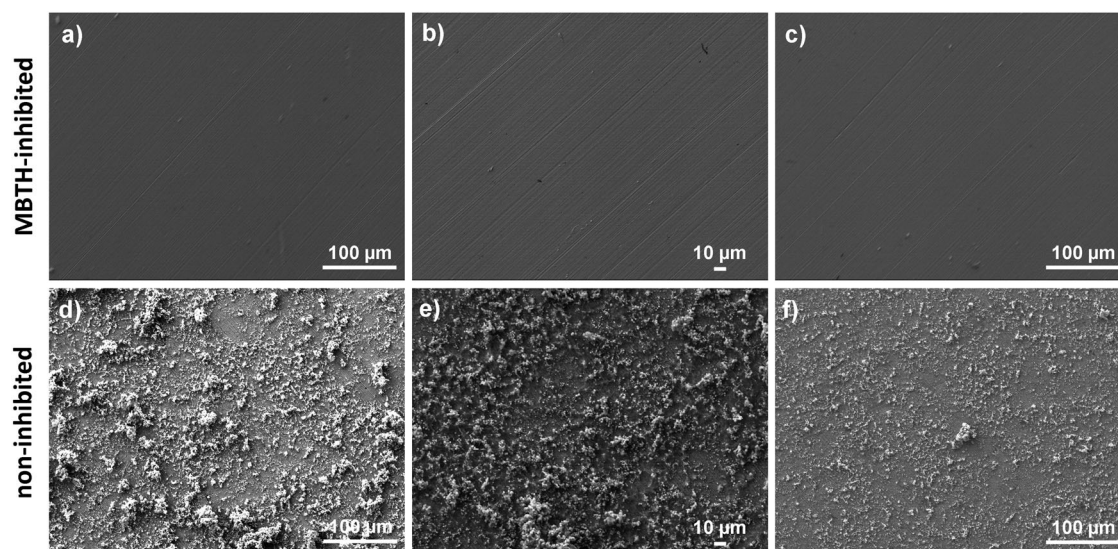


Fig. 1 Morphology. FE-SEM images of brass immersed (a–c) in 3 wt.% NaCl containing 100 ppm MBTH for 31 days and (d–f) in non-inhibited 3 wt.% NaCl for 31 days (three different spots on the surface for both samples).

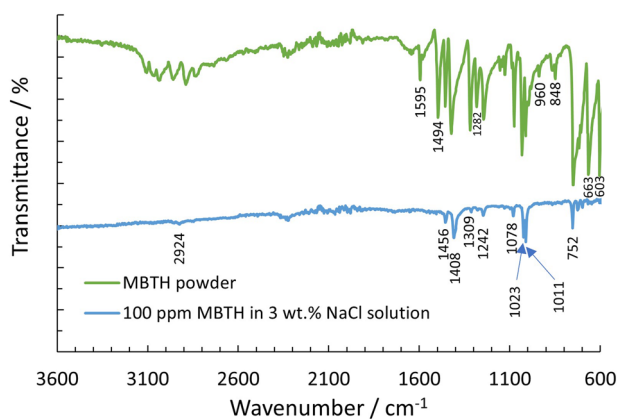


Fig. 2 IR spectroscopy. The ATR-FTIR spectrum measured on a brass sample immersed for 31 days in 3 wt.% NaCl solution containing 100 ppm MBTH and the ATR-FTIR spectrum of MBTH powder (pure chemical).

the MBTH. First, the effectiveness of the corrosion inhibition was tested after 31 days of immersion in a 3 wt.% NaCl solution containing 100 ppm MBTH at $23 \pm 2^\circ\text{C}$. After immersion, the samples were rinsed with ultrapure water and dried under a stream of Ar gas.

Figure 1a–c shows the FE-SEM images of the three different locations on the brass sample, which was immersed for 31 days. The sample exhibited a relatively smooth surface with no significant corrosion damage. Only a uniform pattern of scratches is visible, which were present due to the sample preparation process. On the other hand, the brass sample that was immersed for 31 days in a non-inhibited solution corroded severely, as shown in Fig. 1d–f.

The surface layer that formed during the 31-day immersion period contained MBTH, as confirmed by the ATR-FTIR spectrum in Fig. 2. The peaks at the respective wavenumbers (cm^{-1}) originate from: 2924 (C–H stretching), 1456 (C=N stretching), 1408, 1309, 1023, and 1011 (five-membered ring stretching vibrations)²⁶, 1242 (asymmetric C–O–C vibration)²⁶, 1078 (C–N), and 752 (C–S stretching)^{9,27–29}. For comparison, the ATR-FTIR spectrum for the MBTH powder (pure chemical) is shown. This spectrum contains

additional peaks that are not present or become less intense when the MBTH forms a surface layer after 31 days of immersion in the 3 wt.% NaCl solution containing 100 ppm MBTH. In general, the assignment of the FTIR peaks for azole compounds is challenging³⁰. On the other hand, the ToF-SIMS technique was employed (shown below), which is a molecule-specific technique with a high mass resolution. Therefore using ToF-SIMS, MBTH adsorption was confirmed with much higher confidence compared to ATR-FTIR.

A smooth surface without significant corrosion damage after 31 days of immersion is also confirmed by 3D profilometry and AFM measurements (Fig. 3). The only small island on the 3D profile is presented in Fig. 3a, which could be due to an agglomeration of the MBTH or localized corrosion damage. For comparison, under the same experimental conditions, brass sample immersed in a non-inhibited solution (without MBTH) was severely damaged by the corrosive effect of 3 wt.% NaCl (the 3D profile of this test is shown in ref. ³¹). Moreover, the sample immersed in a non-inhibited solution for 31 days had an average contact angle (θ) of 81.8° (based on three measurements, the results are reported in ref. ³¹), while for the brass sample immersed in a 3 wt.% NaCl solution containing 100 ppm MBTH for 31 days, the average (three measurements) contact angle was 91.4° (Fig. 4). The latter indicates that MBTH increases the hydrophobicity of the surface compared with the brass surface immersed in non-inhibited solution.

Based on the above-mentioned, it can be concluded that the corrosion of brass immersed in a 3 wt.% NaCl solution containing 100 ppm MBTH is greatly mitigated by the corrosion-inhibiting effect of MBTH.

Analysis of the chemical structure of the surface layer

ToF-SIMS and XPS analyses were performed after brass immersion for 1 h in 3 wt.% NaCl solution containing 100 ppm MBTH. The sample was then rinsed with ultrapure water, dried under an Ar stream, and immediately transferred to a spectrometer. The sample prepared as described is hereinafter referred to as MBTH-treated brass. An immersion period of 1 h was chosen to study the initial build up of the surface layer and to be able to measure the substrate-adsorbate connection.

The surface properties of brass immersed in non-inhibited 3 wt.% NaCl solution for 1 h and brass before immersion (after the preparation procedure, as described in Section *Brass sample and*

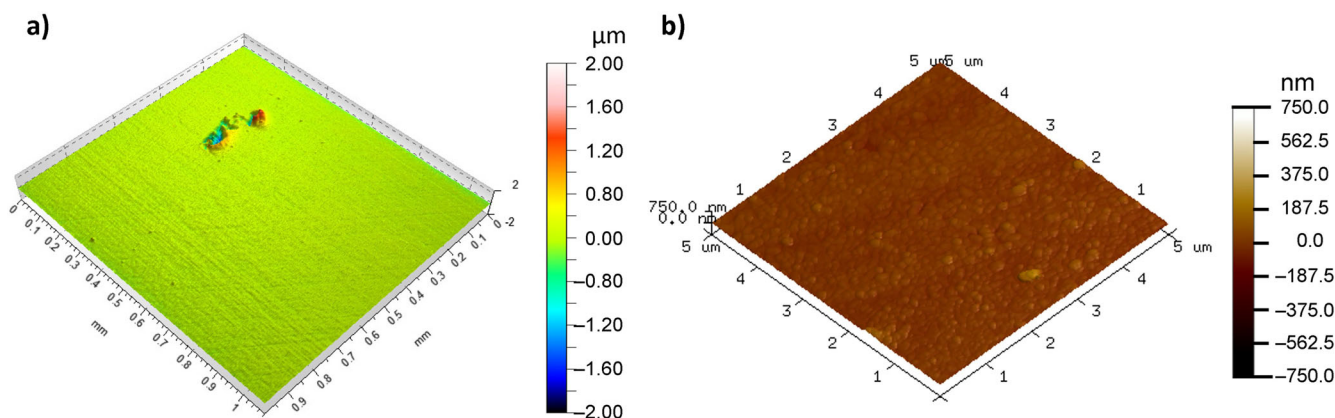


Fig. 3 Topography. **a** The 3D-profile and **b** AFM-image of the brass sample immersed for 31 days in 3 wt.% NaCl solution containing 100 ppm MBTH.

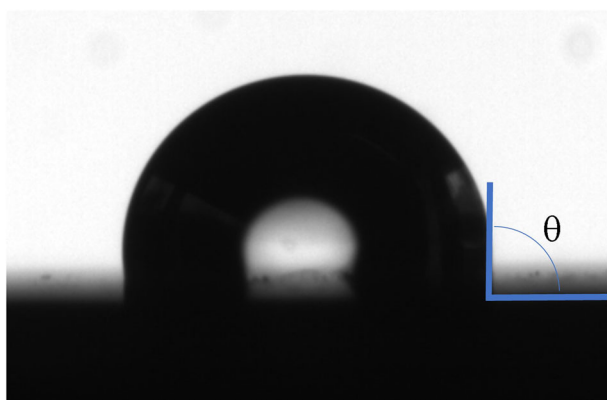


Fig. 4 Hydrophobicity. A photograph of an ultrapure water drop on a brass sample immersed in 3 wt.% NaCl solution containing 100 ppm MBTH for 31 days.

solution preparation) were also tested using XPS and ToF-SIMS techniques. As expected, both techniques confirmed an oxidized brass surface on which adventitious carbonaceous species were adsorbed.

Figure 5 shows negative ion and positive ion ToF-SIMS spectra for MBTH-treated brass in the 0–170 m/z range. Since brass is composed of Cu and Zn, signals for these species are expected on the surface if the organic surface layer (MBTH adsorbed on the surface) is thinner than the analyzed depth of the ToF-SIMS technique. In the negative (Fig. 5a) and positive (Fig. 5b) polarities, the signals for ^{63}Cu and ^{65}Cu are found at m/z 62.93 and 64.93, respectively. Moreover, the signals for ^{64}Zn and ^{66}Zn are present at m/z 63.93 and 65.92, respectively. Therefore, the thickness of the MBTH surface layer is thinner than the analyzed depth of the ToF-SIMS technique. The analyzed depth of the ToF-SIMS technique is ~ 2 nm.

Signals for C^- , CH^- , C_2^- , C_2H^- , C_3^- , C_3H^- , C_4^- , C_4H^- , C_5^- , and C_5H^- (Fig. 5a) and CH_3^+ , C_2H^+ , C_2H_2^+ , C_2H_3^+ , C_2H_5^+ , C_3H_3^+ , C_3H_5^+ , C_3H_7^+ , C_4H_5^+ , C_4H_7^+ , C_4H_9^+ , and C_5H_9^+ (Fig. 5b) represent the mass fragments of the adventitious carbonaceous species that adsorbed on the sample's surface during the sample rinsing, drying, and transfer to the spectrometer. These signals can also arise due to the fragmentation of MBTH. Signals related to the parent ion (M stands for the MBTH molecule) were detected in both polarities, i.e., in the negative polarity for $(M-2\text{H})^-$ at m/z 164.97, $(M-\text{H})^-$ at m/z 165.98, and M^- at m/z 166.98 (Fig. 5a), and in the positive polarity for M^+ at m/z 166.99 and $(M+\text{H})^+$ at m/z

168.00 (Fig. 5b). The presence of these signals, which are related to the parent ion, is strong evidence that the MBTH was adsorbed on the surface. Moreover, the signals designated in Fig. 5a for CN^- at m/z 26.00, S^- at m/z 31.97, CSN^- at m/z 57.98, C_3SN^- at m/z 81.98, $\text{C}_7\text{H}_4\text{NS}^-$ at m/z 134.00, and $\text{C}_7\text{H}_5\text{NS}^-$ at m/z 135.01, and the signals designated in Fig. 5b for C_3HS^+ at m/z 68.98 and C_6H_5^+ at m/z 77.04 are further evidence of the presence of MBTH on the brass surface. In addition, the signals for CNCu_2^+ at m/z 151.87 and Cu_2S^+ at m/z 157.83 in Fig. 5b can be related to the fragments of the organometallic complexes that formed between the Cu ions released due to the corrosion of brass in 3 wt.% NaCl and the MBTH present in solution.

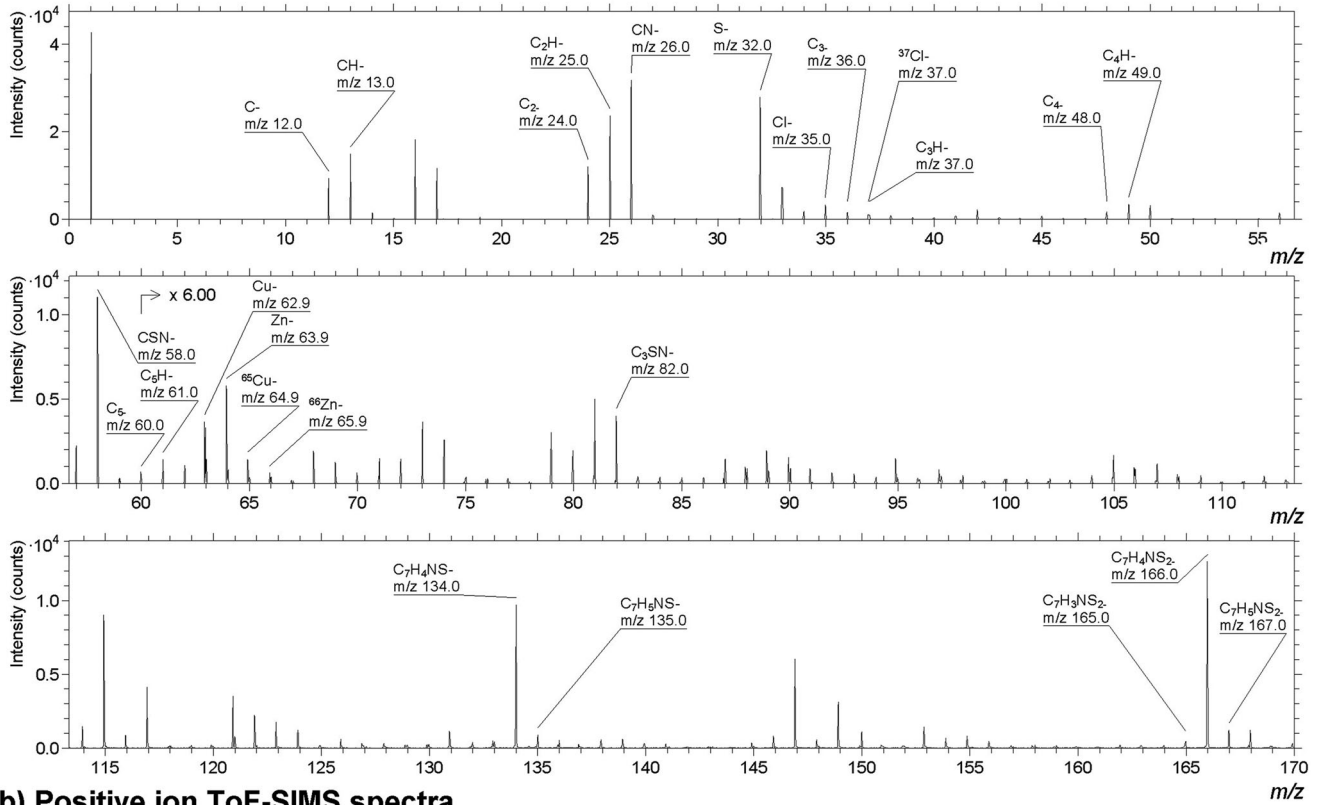
In order to increase certainty (to confirm with a high degree of certainty the presence of MBTH on the surface) tandem (MS/MS) ToF-SIMS is needed. The uncertainty of MS^1 spectra arise due to possible spectral interferences. The precursor ions were transmitted to the collision cell, where fragmentation occurred, before entering the MS^2 analyzer. For all three precursors that can confirm the MBTH molecule, the negative ion MS^2 spectra in Fig. 6 show signals for CN^- , CSN^- , and S_2^- . The precursor ions of $\text{C}_7\text{H}_4\text{NS}_2^-$ and $\text{C}_7\text{H}_5\text{NS}_2^-$ fragment first by releasing 2 S atoms (Fig. 6b, c), while the $\text{C}_7\text{H}_3\text{NS}_2^-$ precursor fragments by releasing NS (Fig. 6a). For the $\text{C}_7\text{H}_3\text{NS}_2^-$ precursor, a signal for C_3SN^- was also determined. Based on the fragmentation products given in Fig. 6, the MBTH structure can be confirmed.

Moreover, various signals for precursor ions were investigated using MS^2 in both polarities, which can represent the formation of organometallic complexes³². Organometallic complexes can form between the MBTH molecules and the Cu or Zn ions released due to the corrosion process³³. Signals for the possible ions that can represent MBTH connected with one or two Cu or Zn ions were considered.

In the positive polarity, the precursor ion for Cu_2M^+ at m/z 293 fragments by releasing the Cu and forming $^{63}\text{CuC}_7\text{H}_5\text{NS}_2^+$ (Fig. 7a). A signal was also determined at m/z 63, indicating $^{63}\text{Cu}^+$. Signals for $^{63}\text{CuC}_6\text{H}_3\text{N}^+$ at m/z 152 and $^{63}\text{Cu}_2\text{S}^+$ at m/z 158 can correspond to MBTH fragments (Fig. 7a). In the negative polarity, a precursor ion for $(\text{Cu}(\text{M}-\text{H}))^-$ at m/z 229 fragments by releasing the ^{63}Cu and forming $(\text{M}-\text{H})^-$, i.e., $^{63}\text{C}_7\text{H}_4\text{NS}_2^-$. The presence of MBTH in the organometallic complex is also characterized by CN^- at m/z 26 (Fig. 7b). Based on the above, the formation of Cu-MBTH organometallic complex is suggested. On the other hand, organometallic complexes that could form between the Zn ions and the MBTH were not identified using the MS^2 capability.

Based on the signals identified as representative of MBTH or its organometallic complexes in both polarities (explained above), the surface distribution of these species was investigated by means of 2D ToF-SIMS imaging. The surface distribution of

a) Negative ion ToF-SIMS spectra



b) Positive ion ToF-SIMS spectra

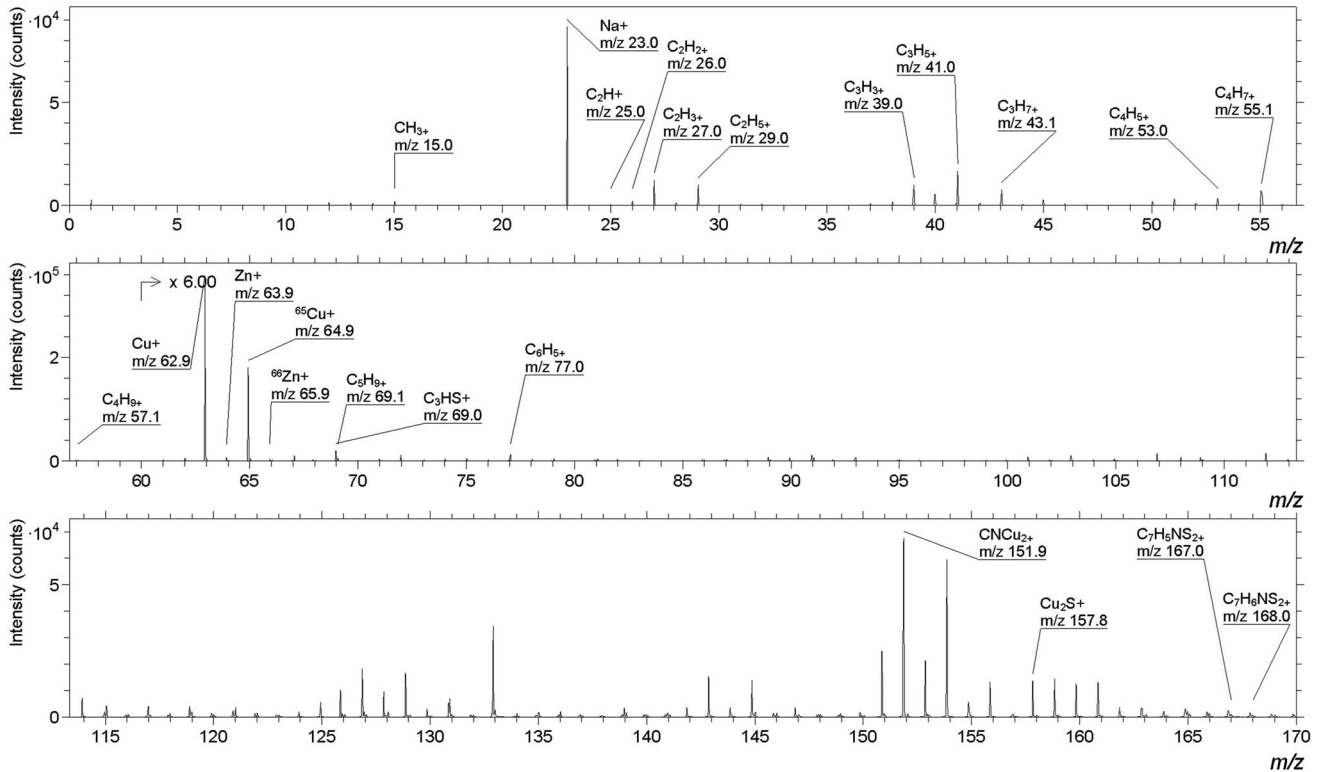


Fig. 5 ToF-SIMS. ToF-SIMS spectra measured in **a** the negative polarity and **b** the positive polarity for the MBTH-treated brass.

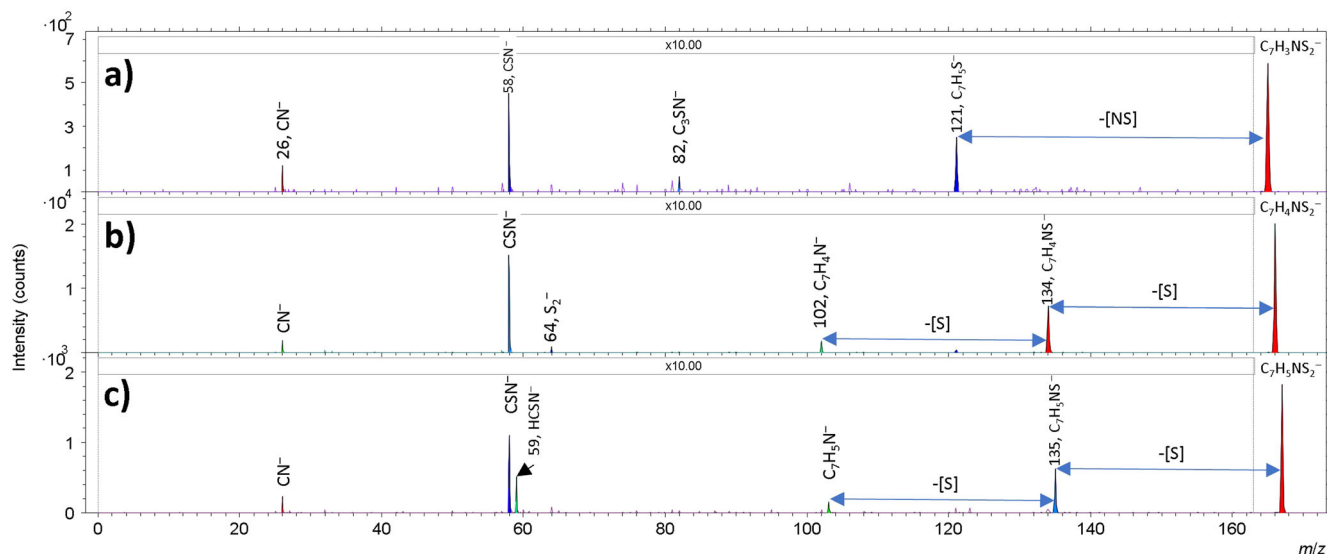
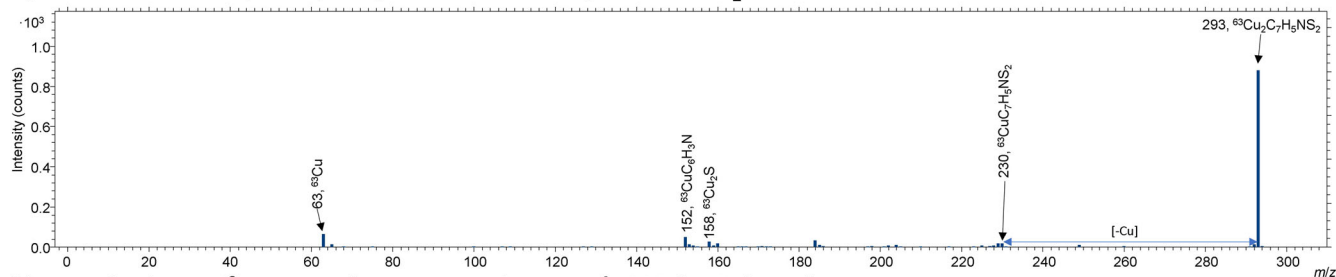


Fig. 6 Tandem ToF-SIMS. The ToF-SIMS MS² negative ion spectra for the **a** C₇H₃NS₂⁻, **b** C₇H₄NS₂⁻, and **c** C₇H₅NS₂⁻ precursor ions.

a) Positive ion MS² spectra; the precursor ion at m/z 293 for Cu₂M⁺



b) Negative ion MS² spectra; the precursor ion at m/z 229 for Cu(M-H)⁻

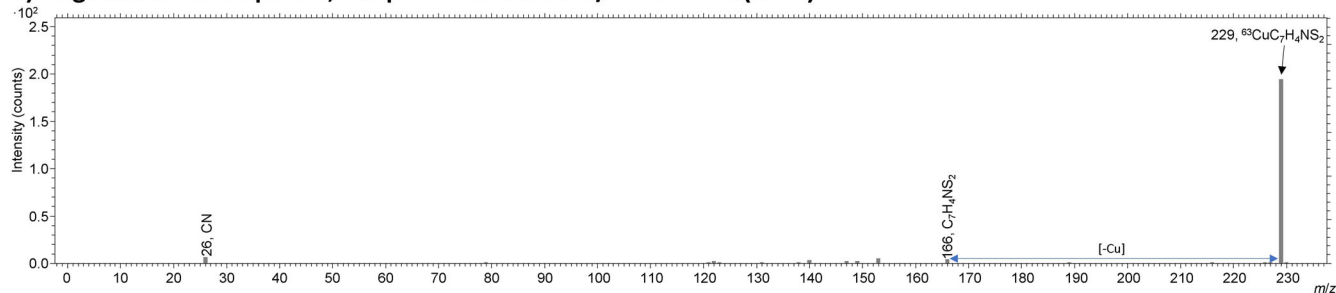


Fig. 7 Tandem ToF-SIMS. The ToF-SIMS MS² **a** positive and **b** negative line spectra for **a** Cu₂M and **b** CuM precursor ions.

corrosion inhibitor molecules is essential to providing effective corrosion inhibition. If the corrosion inhibitor uniformly covers the metallic material, corrosion inhibition is expected to be more effective. On the other hand, uncovered areas are prone to corrosion. The surface of the brass-treated sample was covered mainly by MBTH (Figs. 8 and 9a–c) or its Cu-MBTH organometallic complexes (Fig. 9d). Such surface coverage can explain the high corrosion inhibition effectiveness of the MBTH corrosion inhibitor. A comparison of Figs. 8 and 9 shows that, from the analytical point of view, imaging in the negative polarity is more informative in showing MBTH distribution as the signals are more intense compared to the signals in the positive polarity.

Next, the spatial distribution of MBTH and its organometallic complex with Cu was investigated using 3D ToF-SIMS imaging in the negative polarity (Fig. 10). ToF-SIMS imaging was performed in association with GCIB sputtering. Signals in the negative polarity were used to represent the distribution of surface species, i.e., a

signal for (M-H)⁻ to represent the distribution of MBTH molecules, CuM⁻ to represent the distribution of the organometallic complex, ⁶³Cu⁻ to represent the distribution of Cu-related species (originating mainly from the brass substrate), and ³⁷Cl⁻ to represent the distribution of chlorides on the surface (since the MBTH-treated brass was prepared in chloride solution). The topmost position consists of an organometallic complex (Fig. 10b). MBTH was also present at the same topmost position (Fig. 10a). Moreover, MBTH is also present below the organometallic complex, followed by a mixed and inhomogeneous layer of Cu-related species and chlorides. The signals for Cu-related species and chlorides most likely represent the formation of copper chlorides that formed in the initial stage of brass corrosion when immersed in 3 wt.% NaCl solution containing 100 ppm MBTH.

The survey spectrum of the MBTH-treated brass in Fig. 11 contains signals for Cu (Cu 2p, Cu 3s, and Cu 3p) and Zn (Zn 2p, Zn 3s, and Zn 3p). Cu and Zn also show XPS-excited Auger peaks,

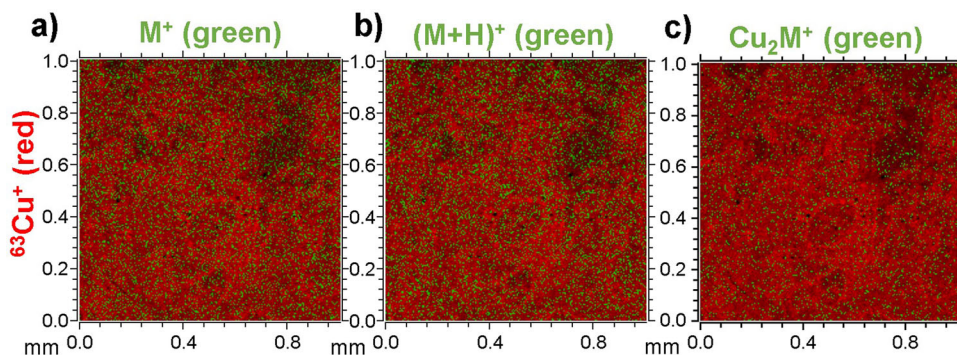


Fig. 8 ToF-SIMS imaging. Positive ion ToF-SIMS imaging; an overlay of signals related to MBTH or its organometallic complex, i.e. **a** M^+ , **b** $(M+H)^+$, and **c** Cu_2M^+ , and the signal related to the brass, i.e. $^{63}Cu^+$.

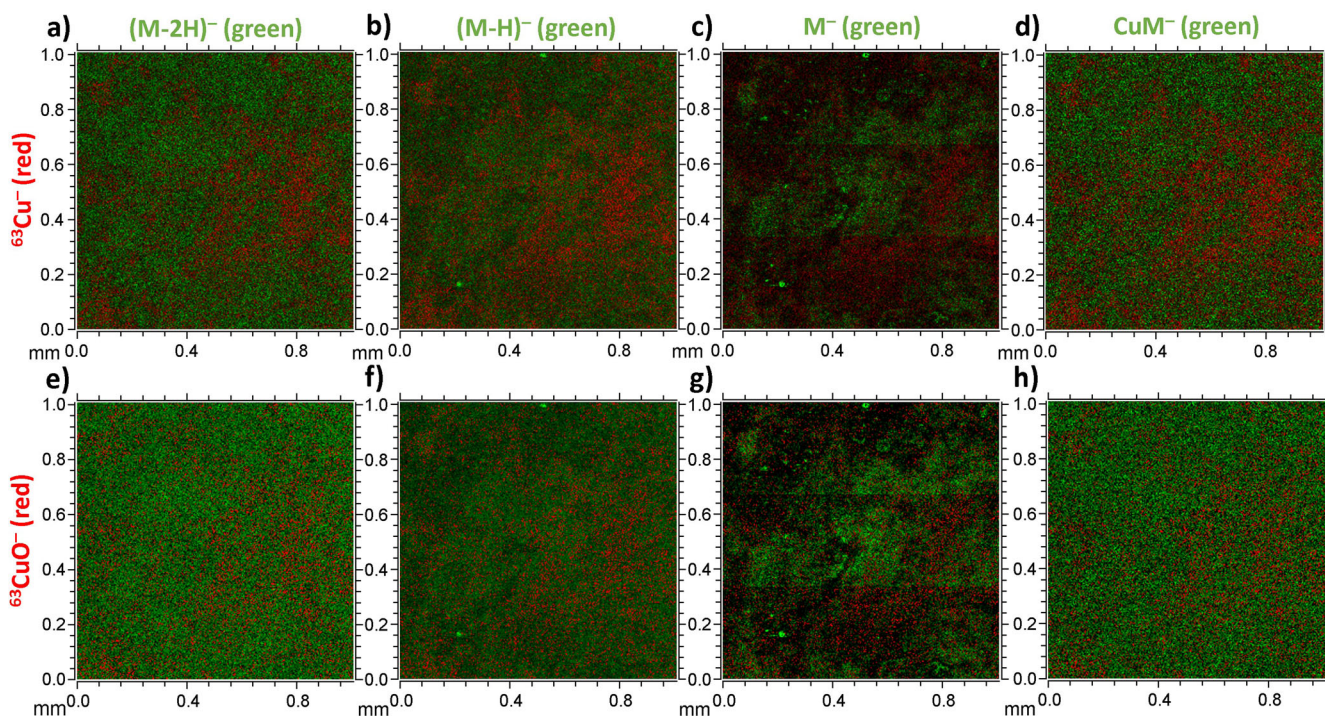


Fig. 9 ToF-SIMS imaging. Negative ion ToF-SIMS imaging; an overlay of signals related to MBTH for **a, e** $(M-2H)^-$, **b, f** $(M-H)^-$, **c, g** M^- , or its organometallic complex for **d, h** CuM^- , and the signal related to the brass; **a-d** $^{63}Cu^-$ and **e-h** $^{63}CuO^-$.

i.e., $Cu L_3M_{4,5}M_{4,5}$, $Zn L_3M_{4,5}M_{4,5}$, and $Zn L_2M_{4,5}M_{4,5}$. The Cu- and Zn-related signals come from the brass substrate or, to a minor degree, from organometallic complexes that formed between the metals and the MBTH. The brass surface is oxidized, and that is why O 1s is detected. Some contribution to the O 1s peak might also come from the oxidized adventitious carbonaceous species or water molecules, which might be hydrogen-bonded to the MBTH layer^{10,34–38}. As the MBTH molecule contains C, N, and S atoms in its structure, the signals for these atoms are therefore detected (C 1s, N 1s, S 2s, and S 2p). A contribution to the C 1s also comes from the adventitious carbonaceous species.

Figure 12 shows the HR XPS spectra obtained during depth profiling with different sputter beams (designated in Fig. 12d). A corresponding depth profile is given in Fig. 13. The topmost position of the surface of the MBTH-treated brass is not rich in Zn (see the Zn concentrations at the beginning of sputtering in Fig. 13), and the Zn 2p spectra are more noisy. When the surface was sputtered with 5 keV Ar_{2000}^+ , 5 keV Ar_{1000}^+ , and 10 keV Ar_{1000}^+ , the surface layer was not significantly removed, and thus

the HR spectra did not change significantly. On the other hand, sputtering with 20 keV Ar_{1000}^+ followed by 20 keV Ar_{500}^+ increased the Zn 2p signal (the noise in the spectra was significantly lower, see Fig. 12a). Consequently, the Zn surface concentration increased (see Fig. 13, evident for the sputtering time from 35 min up to 85 min). When sputtering with monatomic Ar^+ , i.e., 5 keV Ar^+ , the Zn-oxides were removed (simultaneously, the O concentration decreased), and the Zn surface concentration decreased from 23 at.% to approx. 18 at.%. The latter was also associated with minor Zn 2p_{1/2} and Zn 2p_{3/2} peak shifts to more negative E_B (Fig. 12a)³⁹. The XPS-excited Auger Cu $L_3M_{4,5}M_{4,5}$ peaks are (similarly as the XPS-excited Auger Cu $L_3M_{4,5}M_{4,5}$ peaks) susceptible to the Zn environment. They have three distinctive spectral features, designated by dashed lines Nos. 1–3. On the topmost surface, feature No. 3 is the most intense for both Zn $L_3M_{4,5}M_{4,5}$ (Fig. 12b) and Zn $L_3M_{4,5}M_{4,5}$ (Fig. 12c), indicating the presence of ZnO. By sputtering the surface, feature No. 2 increased and became the most intense during sputtering with 20 keV Ar_{500}^+ as ZnO was sputtered off, reaching more metallic Zn⁴⁰.

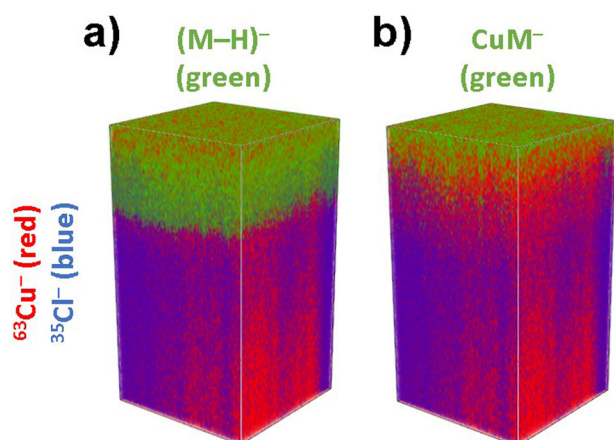


Fig. 10 GCIB-ToF-SIMS. 3D imaging on an analysis area of 300 by 300 μm (in the x- and y-directions shown in the image) associated with GCIB sputtering performed on an area of 500 by 500 μm . The height of these images in the z-direction is not proportional to the scale in the x- and y-directions. **a** The 3D distribution of $(\text{M} - \text{H})^-$ and **b** $(\text{CuM})^-$.

The topmost position (before sputtering) did not contain Cu(II) species because satellites are absent from the $\text{Cu } 2\text{p}$ spectra (Fig. 12d). On the other hand, for the XPS-excited $\text{Cu } L_3M_{4,5}M_{4,5}$ spectra, the intense spectral features at dashed lines Nos. 3 and 4 for the lowest spectra in Fig. 12e (before and after the initial sputtering procedure) indicate that the Cu environment is Cu(I) . The Cu(I) species can originate from the Cu-MBTH complex and Cu_2O . During sputtering and surface layer removal, spectral feature No. 2 became intense as more metallic Cu was obtained. The final sputtering with 5 keV Ar^+ resulted in the characteristic shape of the XPS-excited $\text{Cu } L_3M_{4,5}M_{4,5}$ spectrum, which clearly corresponds to metallic Cu (the four spectral features designated in Fig. 12e)⁴¹.

The HR $\text{O } 1\text{s}$ spectra are shown in Fig. 12f. The topmost species are composed of organic oxygen located at dashed line No. 2. They originate from oxidized adventitious carbonaceous species that were adsorbed on the sample after the preparation procedure and during the sample transfer to the spectrometer. When sputtering, the $\text{O } 1\text{s}$ peak position shifted to a more negative E_B , located at dashed line No. 1, indicating the presence of metal oxides in the deeper subsurface region.

The most intense peak in the HR $\text{C } 1\text{s}$ spectra at E_B of 284.8 eV corresponds to C-C/C-H originating from the benzene ring in the MBTH molecule. C-C/C-H containing species can also originate from the adventitious carbonaceous species. The HR $\text{C } 1\text{s}$ spectra show the shoulder on the high E_B side of the main peak. This shoulder is more pronounced for the topmost species, i.e., the lowest spectra in Fig. 12g. Species contributing to this shoulder can originate from the C-S, C-N, and C-O containing species⁴². MBTH molecule contains one C atom in the five-membered ring that is attached to one N and two S atoms, i.e., $\text{C}(\text{S}_2\text{N})$. Moreover, during the sample preparation, the adsorption of oxidized carbonaceous species containing C-O cannot be excluded. The C-O would also contribute to the high E_B shoulder of the main $\text{C } 1\text{s}$ peak. On that basis, to fit the $\text{C } 1\text{s}$ spectra, four contributions were considered; C-C/C-H from MBTH and C-C/C-H from adventitious carbonaceous species (both will contribute to the main peak at 284.8 eV), and $\text{C}(\text{S}_2\text{N})$ from the five-membered ring of the MBTH molecule and C-O from oxidized carbonaceous species. Both $\text{C}(\text{S}_2\text{N})$ and C-O contribute to the high E_B shoulder of the main $\text{C } 1\text{s}$ peak²¹. The surface atomic concentration of S was determined, as presented in Fig. 13a. As the MBTH molecule contains two S atoms (for which the surface atomic concentration

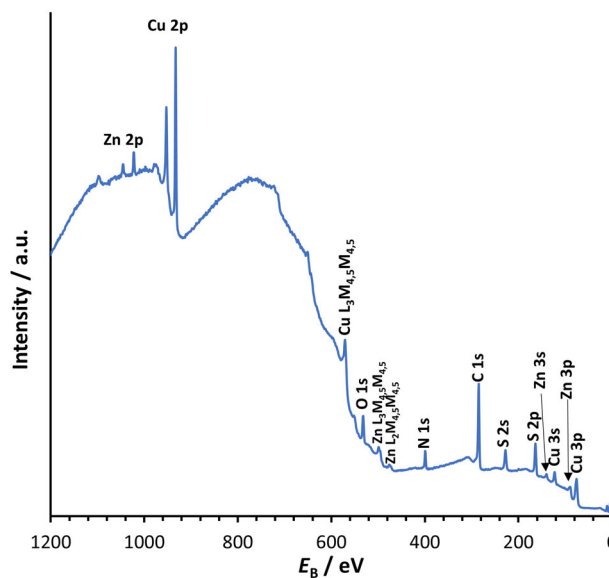


Fig. 11 XPS survey. The survey spectrum for the MBTH-treated brass.

was known) which are attached to one C atom in the five-membered ring, the surface atomic concentration of C atoms in $\text{C}(\text{S}_2\text{N})$ is two-times lower than the surface atomic concentration of S. Consequently, the area of $\text{C}(\text{S}_2\text{N})$ peak in the HR $\text{C } 1\text{s}$ spectra must be considered that the surface atomic concentration of $\text{C}(\text{S}_2\text{N})$ matches with the surface atomic concentration of S after the $\text{C } 1\text{s}$ fitting procedure. Moreover, MBTH contains six C atoms in the benzene ring and one C atom in the five-membered ring. Therefore, the ratio of 6:1 of the areas for the peaks representing these C atoms in the MBTH has been considered in the $\text{C } 1\text{s}$ fitting procedure. The remaining contribution (besides MBTH-related peaks) to the measured $\text{C } 1\text{s}$ spectra comes from C-O and C-C/C-H originating from adventitious carbonaceous species. The $\text{C } 1\text{s}$ spectra were fitted for the measurement before sputtering (Fig. 14a) and after every GCIB sputtering procedure (after all sputtering cycles, Fig. 14b–e). Moreover, the $\text{C } 1\text{s}$ spectrum after the first sputtering cycle using the monoatomic 5 keV Ar^+ sputter beam was also fitted (Fig. 14f).

Based on the peak areas in Fig. 14a, the estimated amounts of C-C/C-H and C-O containing adventitious carbonaceous species before sputtering are 6.9 at.% and 6.7 at.% (relative to the total amount of C-containing species), respectively. Figure 14 shows that the spectral features representing adventitious carbonaceous species became less intense during sputtering with 5 keV Ar_{2000}^+ and 5 keV Ar_{1000}^+ (Fig. 14b, c) and were completely removed from the surface after sputtering with 20 keV Ar_{1000}^+ (Fig. 14d).

The MBTH molecule contains two S atoms and one N atom. The surface atomic concentration of S and N correlates well with the expected S:N ratio of 2 throughout the sputtering procedure in the depth profile until MBTH was present on the surface (Fig. 13b). The MBTH was not removed completely by GCIB, whereas a monoatomic Ar^+ sputter beam was needed to remove the MBTH completely.

The main peak of the HR $\text{N } 1\text{s}$ spectrum in Fig. 12h before the sputtering procedure is located at 399.2 eV (position at the dashed line No. 1), while the main peak of the HR $\text{N } 1\text{s}$ spectrum for pure MBTH chemical (the highest spectrum in Fig. 12h) is located at 400.4 eV (position at the dashed line No. 2). A similar is present for the HR $\text{S } 2\text{p}$ spectra. The main peak in the HR $\text{S } 2\text{p}$ spectra for the pure MBTH molecule is located at 164.0 eV, while the main peak of the HR $\text{S } 2\text{p}$ spectrum for the MBTH-treated sample after the last sputtering cycle with 20 keV Ar_{500}^+ is located at 162.3 eV. These shifts of the main peaks in HR $\text{N } 1\text{s}$ and HR $\text{S } 2\text{p}$ spectra to more

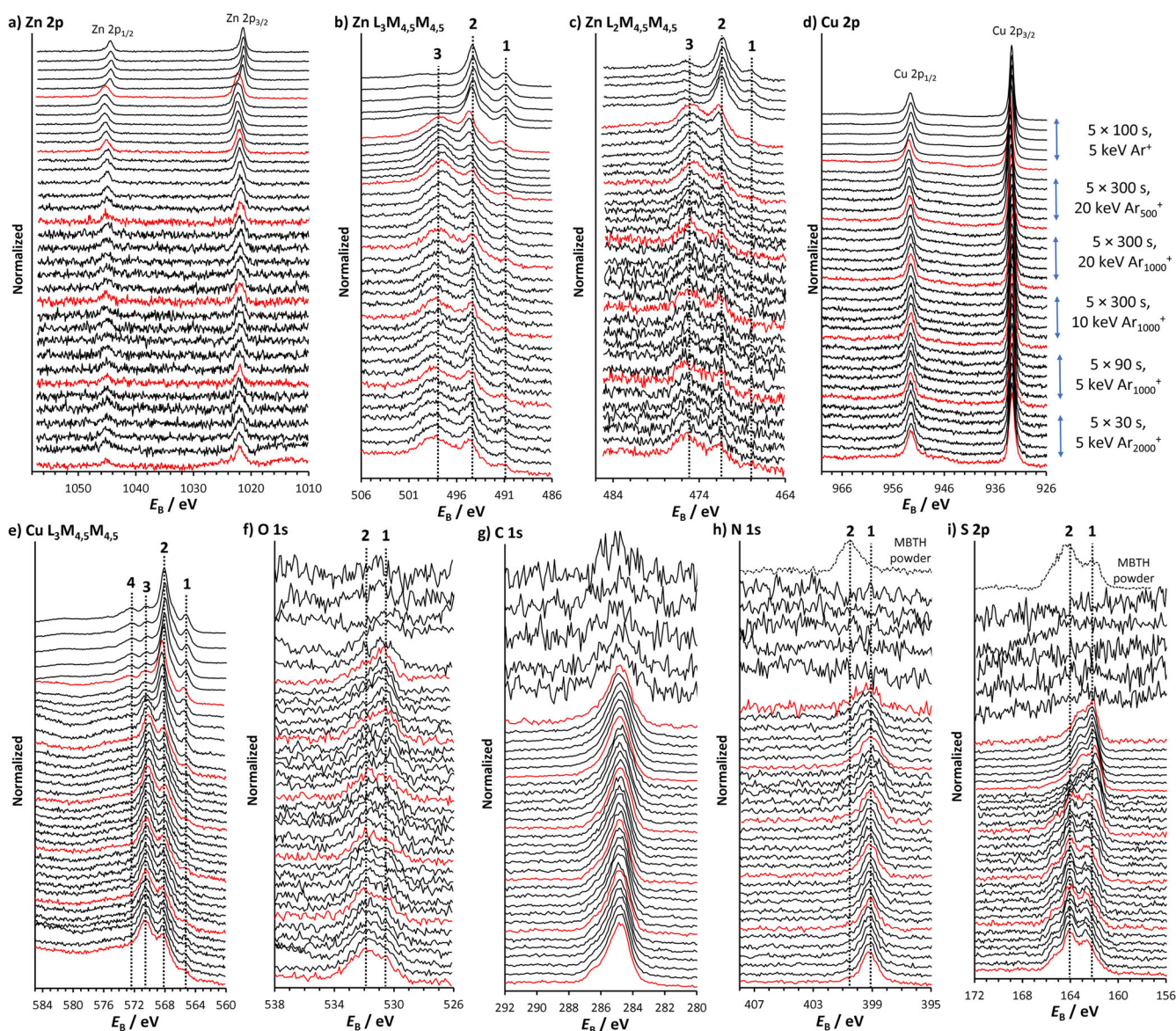


Fig. 12 XPS spectra. HR XPS spectra for **a** Zn 2p, **b** XPS-excited Auger Zn $L_3M_{4,5}M_{4,5}$, **c** XPS-excited Zn $L_2M_{4,5}M_{4,5}$, **d** Cu 2p, **e** XPS-excited Auger Cu $L_3M_{4,5}M_{4,5}$, **f** O 1s, **g** C 1s, **h** N 1s, and **i** S 2p obtained during depth profiling using different acceleration energy and cluster sizes, and monatomic Ar^+ (as designated in **(d)**); red spectra represent the measurement before sputtering). Sputtering is represented from the bottom up (the lowest spectra represent the surface before sputtering).

negative E_B for the MBTH-treated sample compared to the MBTH powder (pure chemical) indicate that N and S atoms are involved in the surface bonding of the MBTH to the brass surface¹⁰.

In general, no peak at an E_B more positive than 166 eV was present in the HR S 2p spectra, indicating that the thiol group in MBTH did not oxidize^{34,43–46}. In addition, the HR N 1s spectra have different peak widths for the location representing the topmost species (the lowest spectra in Fig. 12h) compared to the peaks for the species analyzed during sputtering with 20 keV Ar_{1000}^+ . A peak shape change during sputtering is also present for the HR S 2p spectra in Fig. 12i. In HR S 2p spectra, the most intense peak at 164.2 eV for the topmost species (the lowest spectra in Fig. 12i), located at dashed line No. 2 (the topmost position), shifted to 162.3 eV at dashed line No. 1 after sputtering with 20 keV Ar_{500}^+ . The change in peak shapes and position for HR N 1s and HR S 2p peaks during sputtering indicate different configurations (with different environments of N and S atoms) of the MBTH surface layer located in the topmost position of the surface layer

compared to MBTH molecules closer to the substrate^{20,22}. The same was also reported above using ToF-SIMS measurements, where the topmost position consisted of an organometallic complex along with MBTH molecules, while MBTH molecules were also present below the organometallic complex.

To conclude, this study presents a detailed surface characterization and surface analysis of the corrosion inhibitor 2-MBTH that formed on brass immersed in a 3 wt.% NaCl solution containing 100 ppm MBTH. It was found that the brass sample immersed in a 3 wt.% NaCl solution containing 100 ppm MBTH for 31 days did not corrode significantly, indicating a high corrosion inhibition effect of MBTH. The surface of the brass sample immersed in the MBTH-containing solution had a higher hydrophobic character than the brass sample immersed in non-inhibited solution. Furthermore, ToF-SIMS spectra measurements showed characteristic signals for MBTH molecules, i.e., the signal for $C_7H_3NS_2^-$ ((M-2H)⁻), $C_7H_4NS_2^-$ ((M-H)⁻), and $C_7H_5NS_2^-$ (M⁻), which were also confirmed using tandem (MS/MS) ToF-SIMS measurements based

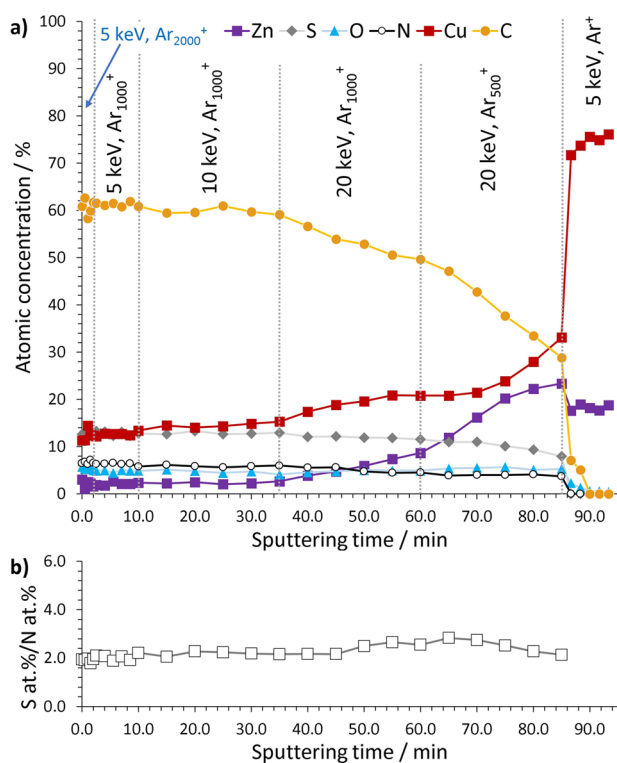


Fig. 13 XPS depth profile. **a** The XPS depth profile obtained based on the measured C 1s, O 1s, S 2p, N 1s, Zn 2p_{3/2}, and Cu 2p_{3/2} HR spectra using different sputter beams, and **b** S at.%/N at.% ratio vs. sputtering time using the same sputter beams as indicated in (a).

on the fragmentation products detected in the MS² spectra. Moreover, ToF-SIMS and XPS measurements indicated the formation of Cu-MBTH organometallic complexes that were produced between the released Cu ions (due to initial stage corrosion) and the MBTH molecules. On the other hand, organometallic complexes that may form between Zn ions and MBTH were not identified. 2D ToF-SIMS imaging showed that most of the surface was covered by MBTH and Cu-MBTH, which explains the reason for the high corrosion inhibition effectiveness of MBTH. ToF-SIMS measurements showed that the very topmost position consisted of organometallic complexes. Under the organometallic complexes, the signal for MBTH was identified, followed by Cu- and Cl-related signals, indicating the presence of copper chloride formed due to the initial corrosion process of brass. The oxidation state of the copper was Cu(I), and no Cu(II) species were formed, as confirmed by XPS measurements. XPS depth profiling using a GCIB and monoatomic Ar⁺ associated with high-resolution spectra measurements indicate that the MBTH bonded to the brass surface via N and S atoms.

METHODS

Brass sample and solution preparation

Brass in the form of 1 mm thick sheets was purchased from Rocholl GmbH (Aglasterhausen, Germany). The supplier reported the composition of the brass as 63.0 wt.% Cu and 37.0 wt.% Zn. From these sheets, the brass samples were cut in the form of discs with a diameter of 15 mm and used for all tests in this study. After cutting, the brass samples were ground under a water jet using a circulating device and SiC papers. Grinding began with Struers (Ballerup, Denmark) SiC paper with 500-grit. The sample was rotated four times to obtain a uniform scratch pattern. After the first grinding with 500-grit paper, the same

procedure was repeated with 800-grit, 1000-grit, 1200-grit, 2400-grit, and 4000-grit SiC paper to obtain a mirror-smooth surface.

After grinding, the surface was thoroughly rinsed with ultrapure water (with a resistivity of 18.2 MΩ cm) and cleaned in an ultrasonic bath for 3 min. with 50.0 vol.% ethanol and 50.0 vol.% ultrapure water. Ethanol (absolute, reagent ISO, reagent Ph. Eur., purity ≥99.8%) was purchased from Merck (Darmstadt, Germany).

The MBTH was dissolved in 3 wt.% NaCl at a concentration of 100 ppm and used as a model medium in this study. The MBTH powder was supplied by Acros Organics, USA (with a purity of 98.0 wt.%), and the NaCl was supplied by Carlo Erba, Italy (pro analysis). The reason for choosing the 100 ppm concentration of MBTH is its limited solubility in 3 wt.% NaCl, where 100 ppm is close to MBTH's solubility limit.

Surface characterization

FE-SEM images were acquired using a JSM-7600F instrument (Jeol, Tokyo, Japan) operated at an accelerated voltage of 15 kV. The 3D profile was measured using a stylus 3D profilometer, model Form Talysurf Series 2 (Taylor Hobson, Leicester, UK). AFM images were acquired using an Innova instrument (Bruker, Karlsruhe, Germany) in contact mode with RTESPA-CP cantilevers (antimony (n) doped Si, Bruker). Contact angle measurements were made with a Krüss DSA 20 tensiometer (Krüss GmbH, Hamburg, Germany). The ATR-FTIR spectrum was measured with a Shimadzu IRAffinity-1 spectrometer (Columbia, MD, USA).

ToF-SIMS analyses

ToF-SIMS spectra measurements, 2D imaging, and 3D imaging were performed with a M6 device (IONTOF, Münster, Germany). As a primary beam, 30 keV Bi₃⁺ was employed at a target current of 0.64 pA.

The spectra were calibrated using the signals at known *m/z*; in the negative polarity, signals for C₃⁻ at *m/z* 36.00, C₄H⁻ at *m/z* 48.00, and C₅H⁻ at *m/z* 61.01 were employed, and in the positive polarity, signals for CH₃⁺ at 15.02 *m/z*, C₂H₃⁺ at *m/z* 27.02, C₃H₇⁺ at *m/z* 43.05, C₄H₇⁺ at *m/z* 55.05, and C₅H₉⁺ at *m/z* 69.07 were used.

The MS² ToF-SIMS spectra were acquired by transferring the precursor ions from the first to the second ToF analyzer. Before entering the second analyzer, the precursor ion was fragmented in the collision cell, which contained He gas at a pressure of 6·10⁻⁶ mbar.

ToF-SIMS 2D imaging was performed by stitching four segments of 500 by 500 μm (each at 256 by 256 pixels) to obtain a final image of 1 by 1 mm. The ToF-SIMS 3D imaging associated with GCIB sputtering was performed using 2.5 keV Ar₂₀₀₀⁺ clusters. Sputtering was performed on an area of 500 by 500 μm and the analysis area was 300 by 300 μm in the center of the sputter crater. The GCIB current measured before sputtering was 51 pA.

XPS analyses

XPS measurements were performed using an AXIS Supra+ device (Kratos, Manchester, UK) equipped with an Al K_α X-ray source. During the measurements, the charge neutralizer was on. Analyses were performed at a 90° take-off angle (with respect to the surface of the samples). The binding energy scale (*E_B*) was corrected using a C-C-H peak at 284.8 eV in the C 1s high-resolution (HR) spectra. The data were acquired and processed with ESCAPE 1.4 software (Kratos, Manchester, UK). Depth profiling was performed using GCIB and a monoatomic Ar⁺ sputter source. GCIB was employed at a different acceleration energy and cluster size, starting with a low acceleration energy and large cluster (a lower acceleration energy per Ar atom in the cluster) and

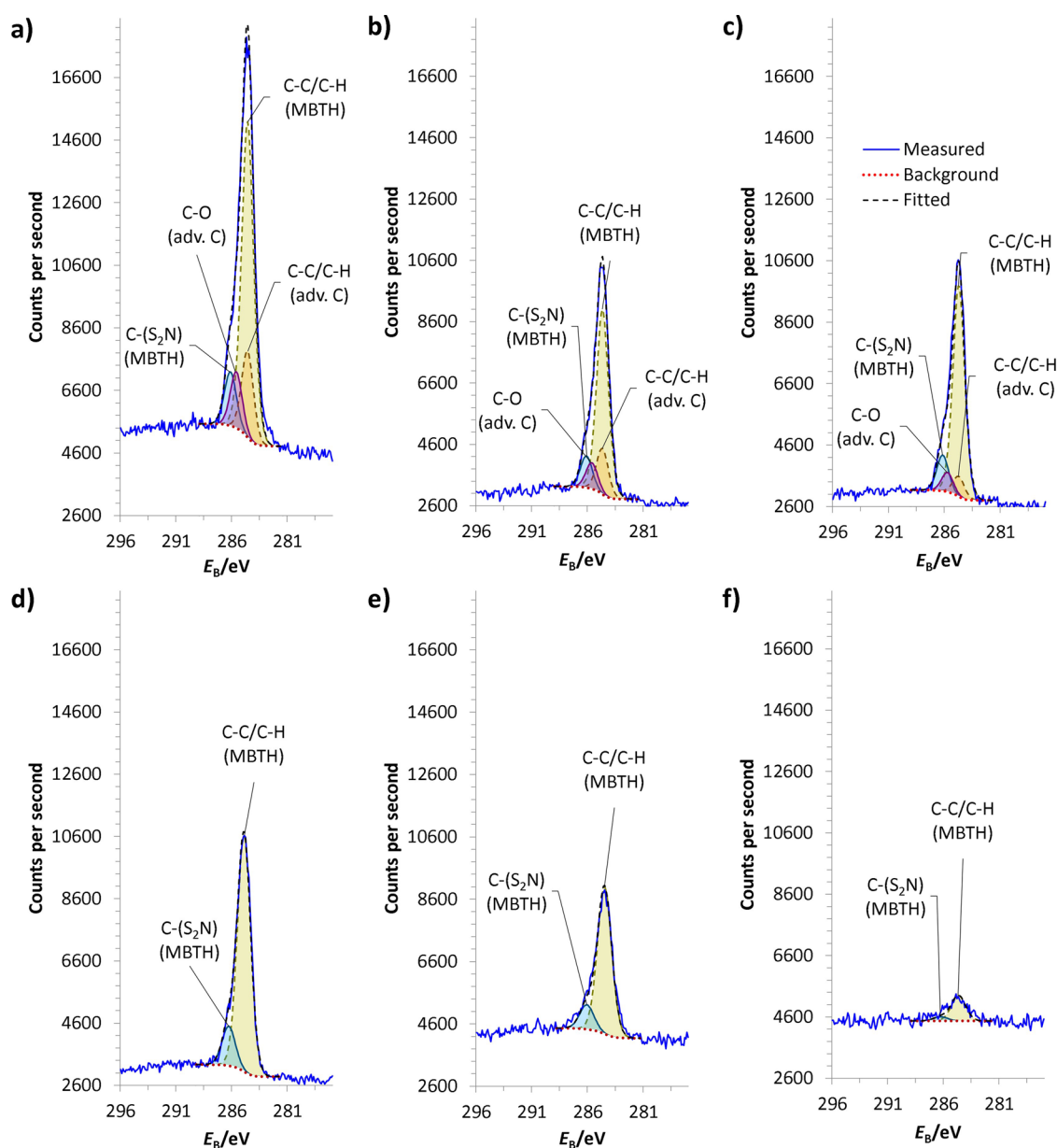


Fig. 14 XPS spectra deconvolution. C 1s fitted spectra; **a** before sputtering, and after sputtering with **b** 5 keV Ar_{2000}^+ for 1950 s, **c** 10 keV Ar_{1000}^+ for 1500 s, **d** 20 keV Ar_{1000}^+ for 1500 s, **e** 20 keV Ar_{500}^+ for 1500 s, and **f** 5 keV Ar^+ for 100 s.

continuing with a higher acceleration energy and smaller clusters, i.e., a higher acceleration energy per Ar atom in the cluster. The depth profile finished with sputtering using monoatomic Ar^+ . The survey spectrum was acquired at a pass energy of 160 eV on a 300 by 700 μm spot size. The HR spectra during depth profiling were acquired at a pass energy of 40 eV on a 110 μm (in diameter) spot size. Cu $2p_{3/2}$, Zn $2p_{3/2}$, C 1s, O 1s, S 2p, and N 1s peaks were employed for quantification after a Shirley background correction⁴⁷.

DATA AVAILABILITY

The data presented in this study are available on request. The data are not publicly available due to technical limitations.

Received: 10 September 2022; Accepted: 21 December 2022;

Published online: 02 January 2023

REFERENCES

1. Cho, S. Y. et al. Finding Hidden Signals in Chemical Sensors Using Deep Learning. *Anal. Chem.* **92**, 6529–6537 (2020).
2. Wang, G., Han, R., Li, Q., Han, Y. & Luo, X. Electrochemical Biosensors Capable of Detecting Biomarkers in Human Serum with Unique Long-Term Antifouling Abilities Based on Designed Multifunctional Peptides. *Anal. Chem.* **92**, 7186–7193 (2020).
3. Ouassir, J. et al. EIS study on erosion-corrosion behavior of BA35 and BA22 brasses in drinking water at various impingement angles. *Coll. Surf. A* **586**, 124151 (2020).
4. Fernández, S. A. & Alvarez, M. G. Passivity breakdown and stress corrosion cracking of α -brass in sodium nitrate solutions. *Corros. Sci.* **53**, 82–88 (2011).
5. Du, X. S., Su, Y. J., Li, J. X., Qiao, L. J. & Chu, W. Y. Inhibitive effects and mechanism of phosphates on the stress corrosion cracking of brass in ammonia solutions. *Corros. Sci.* **60**, 69–75 (2012).
6. Rault, V., Vignal, V., Krawiec, H. & Tadjoa, O. Corrosion behaviour of heavily deformed pearlitic and brass-coated pearlitic steels in sodium chloride solutions. *Corros. Sci.* **86**, 275–284 (2014).
7. Zhang, X., Liu, X., Odneval Wallinder, I. & Leygraf, C. The protective role of hydrozincite during initial corrosion of a Cu40Zn alloy in chloride-containing laboratory atmosphere. *Corros. Sci.* **103**, 20–29 (2016).

8. Marconato, J. C., Bulhões, L. O. & Temperini, M. L. A spectroelectrochemical study of the inhibition of the electrode process on copper by 2-mercaptobenzothiazole in ethanolic solutions. *Electrochim. Acta* **43**, 771–780 (1997).
9. Ohsawa, M. & Suétaka, W. Spectro-electrochemical studies of the corrosion inhibition of copper by mercaptobenzothiazole. *Corros. Sci.* **19**, 709–722 (1979).
10. Chadwick, D. & Hashemi, T. Electron spectroscopy of corrosion inhibitors: Surface films formed by 2-mercaptobenzothiazole and 2-mercaptobenzimidazole on copper. *Surf. Sci.* **89**, 649–659 (1979).
11. Subramanian, R. & Lakshminarayanan, V. Effect of adsorption of some azoles on copper passivation in alkaline medium. *Corros. Sci.* **44**, 535–554 (2002).
12. Tan, Y. S., Srinivasan, M. P., Pehkonen, S. O. & Chooi, S. Y. M. Self-assembled organic thin films on electroplated copper for prevention of corrosion. *J. Vac. Sci. Technol.* **A 22**, 1917–1925 (2004).
13. He, D., Chen, F., Chen, J., Yao, S. & Wei, W. Real-time bulk acoustic wave studies of the inhibition behavior of mercaptobenzothiazole on copper. *Thin Solid Films* **352**, 234–238 (1999).
14. Ramji, K., Cairns, D. R. & Rajeswari, S. Synergistic inhibition effect of 2-mercaptobenzothiazole and Tween-80 on the corrosion of brass in NaCl solution. *Appl. Surf. Sci.* **254**, 4483–4493 (2008).
15. Wu, X., Wiame, F., Maurice, V. & Marcus, P. Effects of water vapour on 2-mercaptobenzothiazole corrosion inhibitor films deposited on copper. *Corros. Sci.* **189**, 109565 (2021).
16. Sharma, S. B., Maurice, V., Klein, L. H. & Marcus, P. Local Effects of Organic Inhibitor Molecules on Passivation of Grain Boundaries Studied in Situ on Copper. *J. Electrochem. Soc.* **168**, 061501 (2021).
17. Chiter, F., Costa, D., Maurice, V. & Marcus, P. DFT investigation of 2-mercaptobenzothiazole adsorption on model oxidized copper surfaces and relationship with corrosion inhibition. *Appl. Surf. Sci.* **537**, 147802 (2021).
18. Chiter, F., Costa, D., Maurice, V. & Marcus, P. Corrosion inhibition of locally de-passivated surfaces by DFT study of 2-mercaptobenzothiazole on copper. *npj Mater. Degrad.* **5**, 52 (2021).
19. Wu, X., Wiame, F., Maurice, V. & Marcus, P. Adsorption and thermal stability of 2-mercaptobenzothiazole corrosion inhibitor on metallic and pre-oxidized Cu(1 1 1) model surfaces. *Appl. Surf. Sci.* **508**, 145132 (2020).
20. Wu, X., Wiame, F., Maurice, V. & Marcus, P. 2-Mercaptobenzothiazole corrosion inhibitor deposited at ultra-low pressure on model copper surfaces. *Corros. Sci.* **166**, 108464 (2020).
21. Wu, X., Wiame, F., Maurice, V. & Marcus, P. Moiré Structure of the 2-Mercaptobenzothiazole Corrosion Inhibitor Adsorbed on a (111)-Oriented Copper Surface. *J. Phys. Chem. C* **124**, 15995–16001 (2020).
22. Wu, X., Wiame, F., Maurice, V. & Marcus, P. 2-Mercaptobenzimidazole films formed at ultra-low pressure on copper: adsorption, thermal stability and corrosion inhibition performance. *Appl. Surf. Sci.* **527**, 146814 (2020).
23. Vernack, E., Costa, D., Tingaut, P. & Marcus, P. DFT studies of 2-mercaptobenzothiazole and 2-mercaptobenzimidazole as corrosion inhibitors for copper. *Corros. Sci.* **174**, 108840 (2020).
24. Chiter, F., Costa, D., Maurice, V. & Marcus, P. Adsorption of 2-mercaptobenzimidazole Corrosion Inhibitor on Copper: DFT Study on Model Oxidized Interfaces. *J. Electrochem. Soc.* **167**, 161506 (2020).
25. Kazansky, L. P., Selyaninov, I. A. & Kuznetsov, Y. I. Adsorption of 2-mercaptobenzothiazole on copper surface from phosphate solutions. *Appl. Surf. Sci.* **258**, 6807–6813 (2012).
26. Bhagyasree, J. B. et al. Vibrational spectroscopic (FT-IR, FT-Raman, ¹H NMR and UV) investigations and computational study of 5-nitro-2-(4-nitrobenzyl) benzoxazole. *Spectrochim. Acta, Part A* **102**, 99–113 (2013).
27. Aparaschivei, R., Şunel, V., Popa, M. & Desbrieres, J. Sulfonic Derivatives of 2-Mercaptobenzoxazole and Its Conjugates with Poly(Maleic anhydride-alt-vinyl acetate) with Potential Pharmacological Applications. *Int. J. Polym. Mater. Polym. Biomater.* **63**, 268–276 (2014).
28. Bhagyasree, J. B. et al. Quantum mechanical and spectroscopic (FT-IR, FT-Raman, ¹H NMR and UV) investigations of 5-nitro-2-phenylbenzoxazole. *J. Mol. Struct.* **1063**, 16–29 (2014).
29. Jiang, X. et al. Effects of non-TR-able codiamines and rearrangement conditions on the chain packing and gas separation performance of thermally rearranged poly(benzoxazole-co-imide) membranes. *J. Membr. Sci.* **564**, 605–616 (2018).
30. Erdogdu, Y., Eskioğlu, B. & Güllüoğlu, M. T. Theoretical investigations on the molecular structure and vibrational spectral analysis of 4-methyl 2-phenylimidazole. *Opt. Spectrosc.* **113**, 596–606 (2012).
31. Finšgar, M. Electrochemical, 3D topography, XPS, and ToF-SIMS analyses of 4-methyl-2-phenylimidazole as a corrosion inhibitor for brass. *Corros. Sci.* **169**, 108632 (2020).
32. Finšgar, M. Advanced surface analysis using GCIB-C60+—tandem-ToF-SIMS and GCIB-XPS of 2-mercaptobenzimidazole corrosion inhibitor on brass. *Microchem. J.* **159**, 105495 (2020).
33. Finšgar, M. & Milošev, I. Inhibition of copper corrosion by 1,2,3-benzotriazole: a review. *Corros. Sci.* **52**, 2737–2749 (2010).
34. Fonder, G., Laffineur, F., Delhalle, J. & Mekhalif, Z. Alkanethiol-oxidized copper interface: the critical influence of concentration. *J. Colloid Interface Sci.* **326**, 333–338 (2008).
35. Chadwick, D. & Hashemi, T. Benzotriazole adsorption on copper studied by X-ray photoelectron spectroscopy. *J. Electron. Spectrosc. Relat. Phenom.* **10**, 79–83 (1977).
36. Duret-Thual, C., Costa, D., Yang, W. P. & Marcus, P. The role of thiosulfates in the pitting corrosion of Fe-17Cr alloys in neutral chloride solution: Electrochemical and XPS study. *Corros. Sci.* **39**, 913–933 (1997).
37. Finšgar, M., Fassbender, S., Hirth, S. & Milošev, I. Electrochemical and XPS study of polyethyleneimines of different molecular sizes as corrosion inhibitors for AISI 430 stainless steel in near-neutral chloride media. *Mater. Chem. Phys.* **116**, 198–206 (2009).
38. Finšgar, M., Fassbender, S., Nicolini, F. & Milošev, I. Polyethyleneimine as a corrosion inhibitor for ASTM 420 stainless steel in near-neutral saline media. *Corros. Sci.* **51**, 525–533 (2009).
39. Moulder, J. F., Stickle, W. F., Sobol, P. E. & Bomben, K. D. *Handbook of X-Ray Photoelectron Spectroscopy*. (Physical Electronics Inc., Eden Prairie, Minnesota, USA, 1995).
40. Biesinger, M. C., Lau, L. W. M., Gerson, A. R. & Smart, R. S. C. Resolving surface chemical states in XPS analysis of first row transition metals, oxides and hydroxides: Sc, Ti, V, Cu and Zn. *Appl. Surf. Sci.* **257**, 887–898 (2010).
41. Finšgar, M. X-ray excited Auger Cu L3L4,5M4,5 spectra measured at low take-off angles as a fingerprint for a Cu-organics connection. *J. Electron. Spectrosc. Relat. Phenom.* **222**, 10–14 (2018).
42. Gengenbach, T. R., Major, G. H., Linford, M. R. & Easton, C. D. Practical guides for x-ray photoelectron spectroscopy (XPS): Interpreting the carbon 1s spectrum. *J. Vac. Sci. Technol.* **A 39**, 013204 (2021).
43. Laibinis, P. E. et al. Comparison of the structures and wetting properties of self-assembled monolayers of n-alkanethiols on the coinage metal surfaces, copper, silver, and gold. *J. Am. Chem. Soc.* **113**, 7152–7167 (1991).
44. Hosseini, M. G., Shahrabi, T. & Nichols, R. J. Characterization of mercaptobenzimidazole adsorption on an Au(111) electrode. *Iran. J. Sci. Technol., Trans. A* **29**, 49–63 (2005).
45. Finšgar, M. 2-Mercaptobenzimidazole as a Copper Corrosion Inhibitor: Part II. Surface Analysis Using X-ray Photoelectron Spectroscopy. *Corros. Sci.* **72**, 90–98 (2013).
46. Finšgar, M. & Kek Merl, D. 2-Mercaptobenzoxazole as a copper corrosion inhibitor in chloride solution: Electrochemistry, 3D-profilometry, and XPS surface analysis. *Corros. Sci.* **80**, 82–95 (2013).
47. Shirley, D. A. High-Resolution X-Ray Photoemission Spectrum of the Valence Bands of Gold. *Phys. Rev. B* **5**, 4709–4714 (1972).

ACKNOWLEDGEMENTS

This work is supported by the Slovenian Research Agency (Grant No. NK-0001 and P2-0118). The project is co-financed by the Republic of Slovenia, the Ministry of Education, Science and Sport, and the European Union under the European Regional Development Fund.

AUTHOR CONTRIBUTIONS

M.F.: Conceptualization; data curation; formal analysis; funding acquisition; investigation; methodology; project administration; resources; software; validation; visualization; roles/writing—original draft; writing—review and editing.

COMPETING INTERESTS

The author declares no competing interests.

ADDITIONAL INFORMATION

Correspondence and requests for materials should be addressed to Matjaž Finšgar.

Reprints and permission information is available at <http://www.nature.com/reprints>

Publisher's note Springer Nature remains neutral with regard to jurisdictional claims in published maps and institutional affiliations.



Open Access This article is licensed under a Creative Commons Attribution 4.0 International License, which permits use, sharing, adaptation, distribution and reproduction in any medium or format, as long as you give appropriate credit to the original author(s) and the source, provide a link to the Creative Commons license, and indicate if changes were made. The images or other third party material in this article are included in the article's Creative Commons license, unless indicated otherwise in a credit line to the material. If material is not included in the article's Creative Commons license and your intended use is not permitted by statutory regulation or exceeds the permitted use, you will need to obtain permission directly from the copyright holder. To view a copy of this license, visit <http://creativecommons.org/licenses/by/4.0/>.

© The Author(s) 2023